

MIT Open Access Articles

Imaging of terahertz fields and responses

The MIT Faculty has made this article openly available. **Please share** how this access benefits you. Your story matters.

Citation: Ofori-Okai, Benjamin K., Prasahnt Sivarajah, Stephanie M. Teo, Christopher A. Werley, and Keith A. Nelson. "Imaging of Terahertz Fields and Responses." Edited by Zhiwen Liu. *Ultrafast Nonlinear Imaging and Spectroscopy II* (September 5, 2014). © 2014 Society of Photo-Optical Instrumentation Engineers (SPIE)

As Published: <http://dx.doi.org/10.1117/12.2063350>

Publisher: SPIE

Persistent URL: <http://hdl.handle.net/1721.1/95526>

Version: Final published version: final published article, as it appeared in a journal, conference proceedings, or other formally published context

Terms of Use: Article is made available in accordance with the publisher's policy and may be subject to US copyright law. Please refer to the publisher's site for terms of use.



Imaging of Terahertz Fields and Responses

Benjamin K. Ofori-Okai¹, Prasahnt Sivarajah¹, Stephanie M. Teo¹, Christopher A. Werley²
and Keith A. Nelson¹

¹MIT Department of Chemistry, 77 Massachusetts Avenue, Cambridge, MA 02139, USA;

²Harvard Department of Chemistry and Chemical Biology, 12 Oxford Street, Cambridge, MA 02138, USA

ABSTRACT

In recent years it has become possible to generate terahertz-frequency (THz) fields that are strong enough to induce nonlinear responses in ordinary molecules and materials. Part of the development of THz technology and nonlinear spectroscopy has relied on optical imaging of THz field profiles and their time and position-dependent evolution. A THz “polaritonics” platform enables extensive control over THz fields that are generated; integration of functional elements such as bandgap structures and metamaterial devices; optical imaging of the THz near and far fields with subcycle temporal and subwavelength spatial resolution; and exploitation of the results for nonlinear spectroscopy. .

Keywords: Terahertz, polaritonics, ultrafast imaging, waveguides, photonic crystals, homogenization, gradient refractive index (GRIN)

1. INTRODUCTION

On-chip control of terahertz (THz) fields in a slab of ferroelectric crystal, termed THz polaritonics¹, has witnessed significant developments in the last 15 years. Using ultrafast pulses, THz fields can be generated in either lithium niobate (LN) or lithium tantalate (LT) through impulsive stimulated Raman scattering². Further control and enhancement of the THz fields are possible by spatial and temporal control of the driving optical fields^{3–5}. It is also possible to introduce a variety of photonic components by machining structures into the slab^{6,7}, or depositing structures on the surface^{8,9}, allowing for further manipulation of THz fields. In addition to these capabilities, the polaritonics platform allows for characterization of the full spatiotemporal evolution of THz waves directly in the slab. By taking advantage of the electro-optic properties of LN and LT, images of the THz waves propagating and interacting with integrated structures can be recorded using time-resolved phase-sensitive imaging¹⁰. This allows for systems and photonic devices to be studied in the near field without the use of external probes. Furthermore, the imaging is carried out using femtosecond optical probe pulses. Thus the THz fields are imaged with deeply subwavelength spatial and sub-cycle temporal resolution.

Here we present recent results on systems built into the polaritonics platform. By taking advantage of the time-resolved imaging, we recorded a series of imaging of THz waves traveling at light-like speeds. The movies contain near-field information about the interaction of the THz waves with the devices built onto the platform which cannot be obtained from far-field measurements. Moreover, the movies can be processed and analyzed to study this behavior at a level of detail that is otherwise unattainable. Although the work focuses on THz frequencies, the scale invariance of Maxwells equations allows for these results to be easily generalized to other areas of the electromagnetic spectrum.

We provide several examples that illustrate the versatility of the polaritonics platform. The first is a gold half-wave antenna that has been deposited on the surface of a slab of LN. Our focus here is on the near-field behavior as the antenna interacts with an incident THz wave. We then illustrate THz wave propagation and our data processing procedure on a plain, unstructured dielectric slab waveguide. Next, we examine the effect of introducing air holes into the slab in the long-wavelength regime, where the composite material may be treated as homogeneous with an effective refractive index, and in the short-wavelength regime where the properties of a

Further author information: (Send correspondence to K.A.N.)

K.A.N.: E-mail: kanelson@mit.edu, Telephone: 1 617 253 1423

photonic crystal slab emerge. In both of these limits and between them, the ability to determine the dispersion properties was critical. Finally, we used the effective index information obtained in the long-wavelength regime to design and study two graded index (GRIN) devices: a Luneburg lens and a bi-directional cloak in a waveguide platform.

2. EXPERIMENTAL DETAILS AND CAPABILITIES

The versatility of the polaritonics platform comes in part from its unique experimental geometry, as illustrated in figure 1. Cylindrical focusing of an intense 800-nm ultrafast near-infrared (NIR) pulse into either a LN or LT slab as a line-source launches counterpropagating THz waves within the slab. The high dielectric contrast between the LN or LT and NIR pulse used for generation, ($n_{LN} \sim 5.1$, $n_{LT} \sim 6.4$ at ~ 1 THz; $n \sim 2.2$ for both LN and LT in the NIR¹) causes the THz field to be emitted as primarily in the lateral directions relative to the optical beam direction even in a bulk crystal¹¹. The subwavelength thickness of a LN or LT slab causes the THz waves to remain waveguided within the slab. Aligning the polarization of the NIR pulse along the optic axis of the crystal creates THz waves that are polarized with the electric field (E-field) parallel to the air-crystal interface and perpendicular to the propagation direction, or TE-polarized. As LN and LT are both electro-optic materials, the index of refraction changes by an amount $\Delta n(y, z)$ which is directly proportional to the THz E-field. Thus an imaging method that records the optical refractive index variation in the plane of the slab reveals the THz E-field profile.

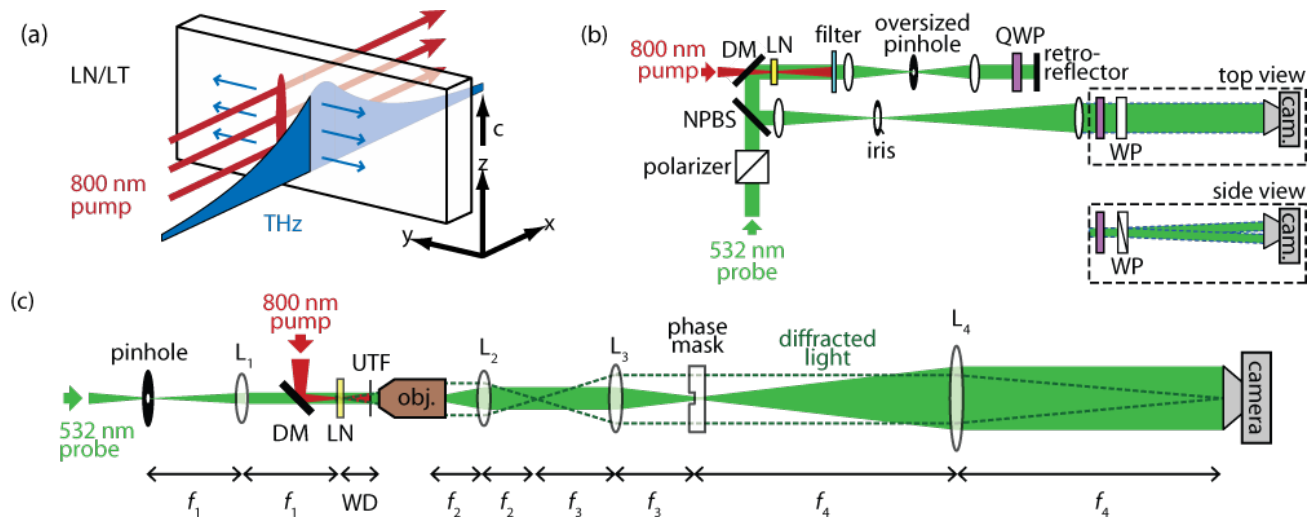


Figure 1. (a) Schematic representation of the polaritonics platform. A cylindrically focused femtosecond 800-nm line-source pump pulse (red) passes through a thin slab of x -cut LN or LT crystal launching a THz waveguide mode response (blue) which travels away from the point of generation. The waveguide mode depicted is the lowest order TE mode of the bare slab. (b) Schematic illustration of the polarization gating imaging setup. By using a quarter wave plate (QWP) and Wollaston Prism polarizer (WP), the spatially dependent information from the probe is mapped onto an intensity change while the crystal is simultaneously imaged using a 2-lens 4f imaging system. (c) Schematic illustration of the phase contrast imaging setup. In this system, phase to intensity conversion occurs through the use of the phase mask. The phase mask introduces a $\pi/2$ phase shift between light which passes unperturbed through the slab and light which diffracted off the THz waves. Interference between the two components in the image plane leads to the required phase-to-intensity conversion.

In order to measure the spatially dependent index of refraction, an expanded 532 nm probe pulse, which is generated from a noncollinear optical parametric amplifier and is time delayed relative to the NIR pump pulse, is passed through a large section of the crystal and in doing so acquires a spatially dependent phase shift, $\Delta\phi(y, z) = 2\pi \frac{\ell}{\lambda} \Delta n(y, z)$, where ℓ is the thickness of the crystal and λ is the wavelength of the probe. This phase shift cannot be measured directly on a camera, but must first be transformed into an intensity modulation. This

is accomplished using either the polarization gating imaging or phase contrast imaging technique¹⁰, represented schematically in figures 1(b) and (c), respectively. Both methods generate images in which the intensity of the probe is modulated due to the relative phase shift $\Delta\phi$. Through Jones calculus¹², one can find that the relative change in the intensity, $\frac{\Delta I}{I_0}(y, z)$, is directly proportional to the induced phase change, $\Delta\phi(y, z)$, which is in turn proportional to the THz E-field. For both of the methods described above, femtosecond pulses at visible wavelengths are used to record movies of the THz waves. As a result, the imaging resolution is set by the optical diffraction limit and is highly subwavelength ($\sim \lambda/100$) relative to the THz wavelength. In phase contrast, the imaging resolution is $\sim 1.5 \mu\text{m}$, while in polarization gating the resolution is $< 5 \mu\text{m}$, making it possible to observe near-field behavior directly.

The near-field imaging capability of the polaritonics platform is demonstrated in figure 2, which shows a series of images recorded using phase contrast imaging of THz waves interacting with an antenna pair. Each antenna arm is a gold pad that is roughly $60 \mu\text{m}$ wide and $100 \mu\text{m}$ tall that has been lithographically deposited on the surface of a LN crystal. The frequency of the THz wave has been set to 530 GHz using spatiotemporally shaped driving fields⁵ rather than a cylindrically focused line-source. 530 GHz was chosen as it corresponds to a high order resonance of the antenna. As the multicycle THz wave encounters the antenna, the evanescent portion of the THz E-field that is outside of the slab causes electrons to oscillate and form a near-field mode pattern with a vertical node bisecting the arms and with multiple horizontal nodes. The near-field enhancement of the THz field amplitude at the edges of the antenna can be observed (see figure 2(c)), as well as the $\pi/2$ phase shift between the incident wave and the field in the gap between the antennas (figures 2(d) and 2(e)). As the antenna interacts with the THz wave, it ultimately radiates back into the far field which is most clearly visible in figure 2(e).

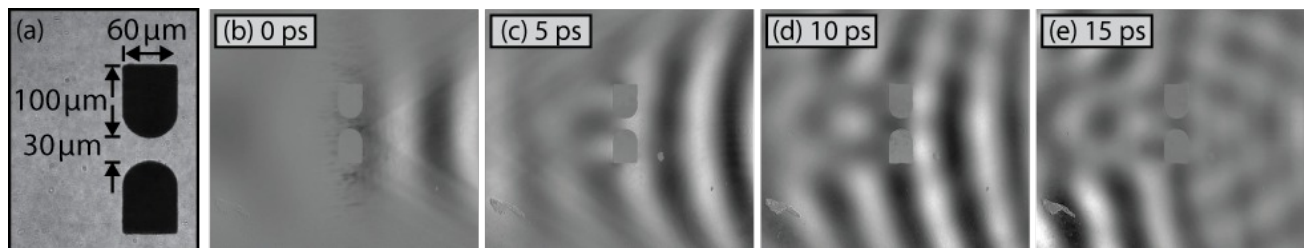


Figure 2. (a) Illustration of the near-field imaging capabilities of the polaritonics platform. (a) Dimensions of the gold antenna that was deposited onto the LN slab surface. The dimensions of the antenna are much greater than the imaging resolution, making it possible to easily observe near-field behavior. (b)-(e) A time series of images showing the multicycle THz wave interacting with the antenna and the resulting far-field radiation pattern.

In addition to capturing the near-field behavior, the images can be analyzed to study THz wave propagation behavior, as is illustrated in figure 3. Figure 3(a) shows several images of THz waves propagating within an unstructured slab of LN crystal. After 10 ps, two counterpropagating waves that were generated using a cylindrically focused line-source pump pulse are clearly visible. As time progresses, the waves travel farther apart and there is evidence of waveguide dispersion as well as waveguide mode separation. While the movie captures the full spatiotemporal evolution of the THz waves, it can be more compactly represented in a space-time plot, as shown in figure 3(b). This plot is obtained by taking a frame of the movie and averaging over the vertical dimension along which the field is uniform. This collapses the 2D frame into a 1D vector containing the horizontal spatial information of the THz field at one point in time. This is done for each frame of the movie and the resulting 1D vectors are stacked vertically in time order, generating a 2D matrix where the x-axis represents position while the y-axis represents time as shown in figure 3(b). Performing a double Fourier transform of the space-time plot converts position to wave vector and time to frequency, thereby generating the dispersion curve as shown in figure 3(c).

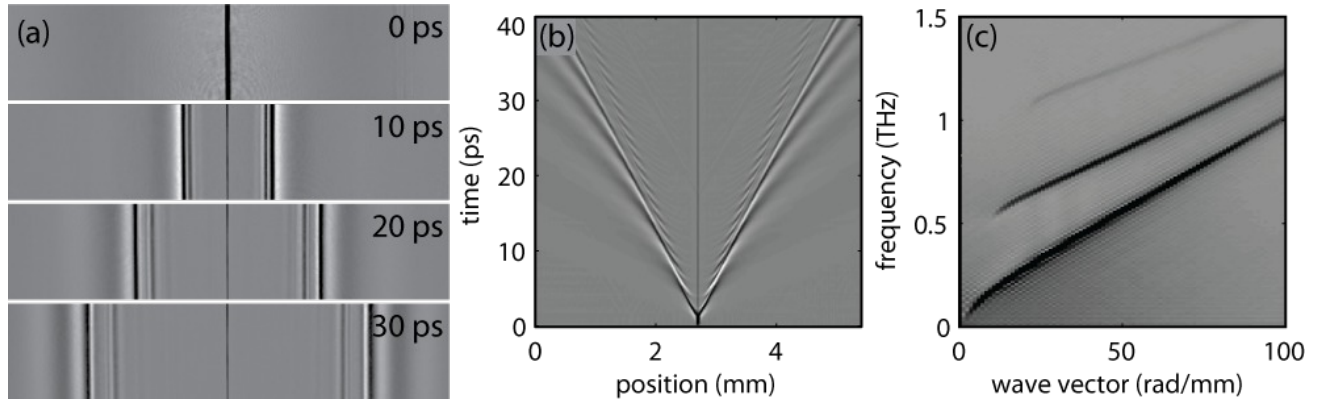


Figure 3. (a) Examples of images of THz waves propagating within a bare $54 \mu\text{m}$ thick LN slab. At various time delays the waves have clearly separated. (b) Space-time plot representation of the data. The space-time plot displays the full spatiotemporal evolution of the THz field. (c) Wave vector-frequency dispersion curves obtained by taking a 2D Fourier transform of the space-time plot in (b). Three waveguide modes are clearly visible in the dispersion diagram.

3. UNDERSTANDING HOMOGENIZATION BREAKDOWN

Under appropriate conditions, a complex optical system comprised of multiple elements such as an array of holes or inclusions in a host dielectric can be approximated as a homogenous composite material with an effective refractive index¹³. Despite its widespread application in the design of graded index (GRIN) devices and transformation optics^{14,15}, the range of applicability of the homogenization approximation has not been well quantified. For a composite material to be treated as homogenous, the wavelength λ of light must be sufficiently large compared to the characteristic size d of the structure or inclusion or of the period in a repeating pattern^{16,17}. Typical experiments operate with $\lambda/d \sim 5$ to 10 ¹⁸⁻²⁰, yet simulations have shown that the homogenization approximation may be valid even with the ratio as small as 2.3 ²¹. The condition becomes further unclear in waveguides where the wavelength of light can be on the order of the structure or inclusion thickness, requiring full 3D simulations to treat the geometry. Understanding where homogenization theory applies can allow for analytical formulas to be used with the effective index as a parameter, enabling rapid device design and prototyping without the need for extensive simulations.

To investigate the limits of the homogenization, lattices of air holes were cut into LN and LT slabs using a hydrofluoric acid etch-assisted laser machining process²². Movies of THz wave propagation recorded and analyzed to extract the dispersion curves for these systems. Figure 4(a) shows the experimental dispersion curve (blue) for a truly homogenous, $54 \mu\text{m}$ thick bare slab of LT. The experimental dispersion curve shown was extracted from a plot similar to the one shown in figure 3(c). Overlaid on figure 4(a) is a numerically calculated waveguide dispersion curve¹² where the refractive index, n , was adjusted to 6.44, yielding a faithful reproduction of the experimental dispersion curve. Figure 4(b) shows the corresponding dispersion curve (blue) for the same LT waveguide after it was patterned by cutting a square lattice of air holes through the slab (see figure 4(b) inset). We similarly overlay on figure 4(b) a numerical waveguide dispersion curve (green) with a refractive index determined by optimizing the fit to the experimental curve at long wavelengths ($\lambda \gg$ lattice spacing).

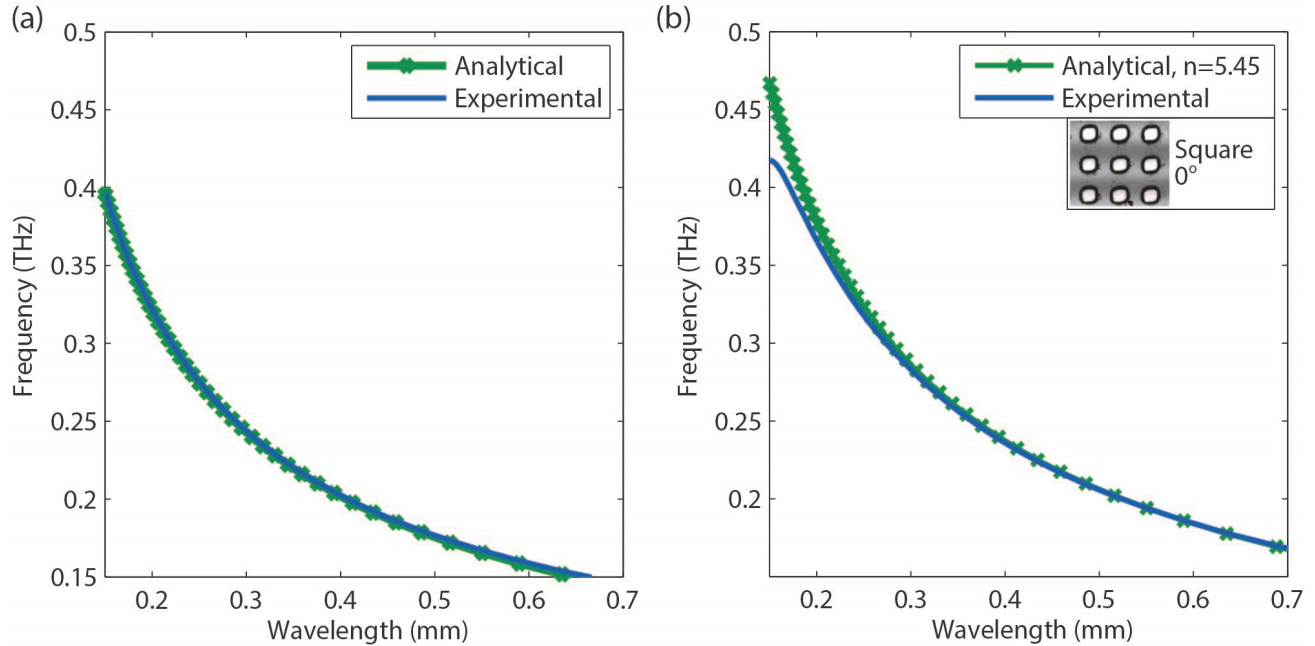


Figure 4. Dispersion curves reveal breakdown of homogenization. (a) Experimental dispersion curve for a bare slab of $54 \mu\text{m}$ LT. The overlaid numerical waveguide dispersion curve demonstrates agreement at all wavelengths in a truly homogenous material. (b) Dispersion curve for a composite waveguide with hole radius of $26 \mu\text{m}$ and lattice spacing of $100 \mu\text{m}$, shows good agreement to a fitted numerical waveguide curve at long wavelengths (above $\lambda_{cutoff}=260 \mu\text{m}$) where the composite waveguide can be considered homogenous with a single effective index. Deviation between the numerical fit and the experimental curve demonstrates breakdown of the homogenization approximation. Inset shows magnified view of the composite waveguides lattice.

Agreement between experimental data and the fitted numerical curve at long wavelengths suggests that the composite waveguide can be treated as a homogenous slab with an effective index of $n_{eff}=5.45$ in this regime. However, at small THz wavelengths the effect of each individual scatterer is prominent and photonic bandgap properties are present. Where the percent difference in frequencies between the numerical and experimental frequencies reaches 5%, we define the cutoff wavelength, λ_{cutoff} , as the lower bound below which the composite waveguide can no longer be treated as homogenous. In this particular case, we observed $\lambda_{cutoff}=260 \mu\text{m}$. In general, we found that if the wavelength in the waveguide is at least twice as large as the Bragg condition wavelength¹², the homogenization approximation is valid in these composite structures and remains independent of the detailed geometry, material, or fill fraction. We also found that the effective refractive index can be accurately predicted using the Maxwell-Garnett mixing formula²³, meaning that this can be used to quickly design a GRIN device by simply varying the size and density of the air holes.

4. ANALYZING WAVE BEHAVIOR IN PHOTONIC CRYSTAL SLABS

Photonic crystals (PhC) have emerged as versatile tools for controlling radiation across the electromagnetic spectrum²⁴. They are a special class of mixed dielectric materials, in which the different components have been arranged in a periodic manner with a lattice constant d on the order of half the wavelength of light of interest $\lambda/2$ where the periodic structures can no longer be treated as homogenous. Beyond this point, the material develops unique dispersion relations not present in homogeneous materials as well as the photonic band gap, i.e. a range of frequencies for which light cannot propagate inside the PhC^{25,26}. These properties have made it possible for photonic elements such as routers²⁷ and filters^{28,29} to be fabricated based on the PhC architecture.

In order to study THz wave propagation in these systems, PhC slabs were patterned into a slab of LT. Figure 5(a) shows a series of images of THz waves propagating within a PhC composed of air holes with radius

$r = 35 \mu\text{m}$ arranged into a square lattice with a lattice constant of $100 \mu\text{m}$. When the rightward-moving wave reaches the PhC, the frequencies within the photonic band gap are strongly reflected. The waves with frequencies outside the photonic band gap enter the PhC slab and couple to both TE-like and TM-like modes of the PhC slab and continue to propagate through the structure. We can also clearly see evidence of dispersion as different frequency components propagate at different speeds. The THz waves in the PhC also travel at a different velocity compared to the unstructured slab³⁰, further demonstrating distinct dispersion relations.

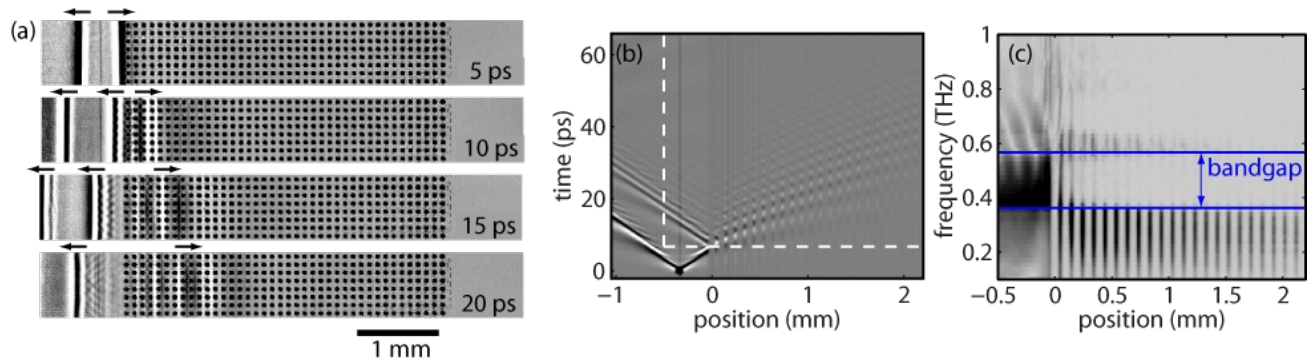


Figure 5. (a) A series of images showing THz wave propagation through a square PhC with a lattice constant of $100 \mu\text{m}$. The air holes are false-colored black in post-processing for clarity. The black arrows at the top indicate the wave propagation directions, revealing the wave reflected by the PhC starting at 10 ps. (b) A space-time plot generated by averaging over the vertical dimension of the frames in the movie. The strong band gap reflection can be seen when the rightward wave encounters the PhC structure, which starts at position 0 mm. (c) A space-frequency plot resulting from a Fourier transform along the time axis of the portion of (c) enclosed by the dashed white lines. Waves with frequencies outside the band gap are allowed to propagate within the PhC while those in the band gap only penetrate a short distance.

The space-time plot obtained from this measurement is shown in figure 5(b). When the rightward-propagating wave encounters the edge of the PhC lattice at 0 mm, some of the wave is reflected while the rest continues into the PhC. The positions in the space-time plot where the signal is smaller (vertical gray bars cutting through the wave) occur because of the air holes. Since the THz waves can only be detected in LT, vertical averaging over the air holes reduces the signal at those positions. Photonic band gaps can be determined from space-frequency plots like the one shown in figure 5(c), which are calculated by Fourier transforming the space-time plot in figure 5(b) along the time axis. As observed in figure 5(c), frequencies within the photonic band gap (between 0.36 ± 0.02 and 0.54 ± 0.01 THz) are reflected efficiently and only penetrate a short distance into the PhC. Theory predicts that inside the PhC, waves within the band gap decay exponentially due to coherent reflections²⁴. They can be described as having complex propagation wave vectors $\kappa = \kappa + i\gamma$. This behavior was also examined by fitting the amplitude of the field with a frequency of 0.47 THz inside the PhC to the function $A \cdot \exp(-y/Y)$, yielding a decay constant of $Y = 90 \pm 3 \mu\text{m}$. This value deviates substantially from the value of $71 \mu\text{m}$ obtained by simulation. The short decay length is due to the high index contrast between LT and air.

To complete our study, we analyzed movies of THz waves propagating in different PhC lattices in order to map out their full dispersion diagrams. The resulting diagrams are shown in figure 6. As expected, the dispersion within the PhC depends strongly on the direction of wave propagation relative to the principal lattice vectors of the periodic structure. The signals that are observed in the measured dispersion diagram correspond to eigenmodes, represented with solid red lines, and leaky modes of the PhC.

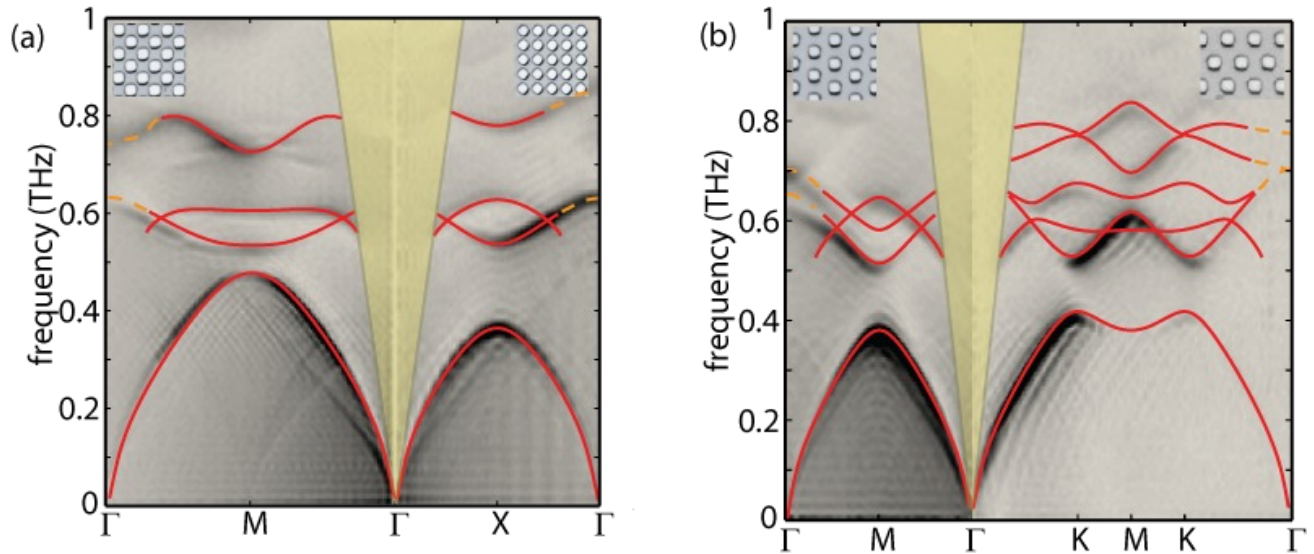


Figure 6. Dispersion diagram for PhC slabs with a square lattice (a) and a hexagonal lattice (b). For the square lattice, the lattice constant $a = 100 \mu\text{m}$ and the hole radius $r = 35 \mu\text{m}$. For the hexagonal lattice, $a = 100 \mu\text{m}$ and $r = 25 \mu\text{m}$. Rotation of the square lattice by 45° switches the THz propagation vector between Γ -X and Γ -M (see inset). For the hexagonal lattice a rotation of 90° switches the THz propagation vector between Γ -M and Γ -K-M (see inset). Analytical solutions of eigenmodes (solid red lines) and leaky modes (dashed orange lines) with the appropriate symmetry are overlaid on top of the data. The triangular regions highlighted in yellow represent the modes in the light cone.

5. GRADIENT REFRACTIVE INDEX DEVICES

Under the homogenization approximation, one can specify the 3-dimensional index of refraction, $n(x, y, z)$ by controlling the spatially varying size, density, or type of inclusions; this has found widespread application in the form of GRIN devices. Using the homogenization condition and the Maxwell-Garnett mixing formula, we designed and fabricated a Luneburg lens³¹ and cloak in the polaritonics platform. We then used time-resolved imaging to record THz fields moving inside the devices, offering direct insight into device operation.

The first device studied was a rotationally symmetric lens (see figure 7(a)), known as a Luneburg lens. Unlike conventional lenses, the Luneburg lens is capable of focusing a plane wave incident from any direction to a point on the other side of its surface. Figure 7 shows the time evolution of a THz wave with a wavelength of $\lambda=300 \mu\text{m}$ as it passes through the lens. As the THz waves propagates within the lens, the curvature of the wave front changes (compare figures 7(a) and 7(b)) leading to focusing of the wave on the lens surface (figure 7(c)). The operation of the device is encouraging, with a focal spot size of $\sim 200 \mu\text{m}$ that is slightly larger than the diffraction limit of $\lambda/2=150 \mu\text{m}$ that would be reached in an ideal Luneburg lens¹⁶. The incomplete focusing can be attributed to the curvature and finite bandwidth of the incoming THz field that result from the multicycle THz wave generation process.

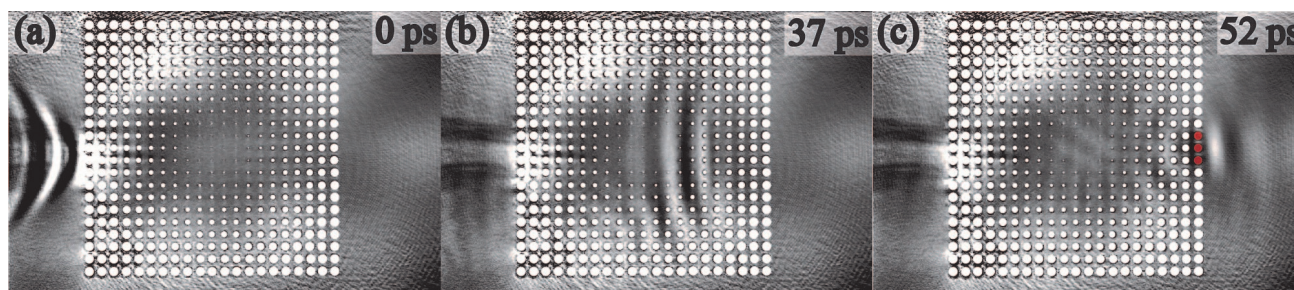


Figure 7. A Luneburg lens in a $54 \mu\text{m}$ LT waveguide, focusing a multicycle THz wave of center wavelength $\lambda=300 \mu\text{m}$. Air holes have been artificially masked in white for clarity. (a) Incoming THz wave (b) Change in curvature of the beam once it enters the lens after 37 ps (c) Focused THz wave with spot size of $200 \mu\text{m}$ after 52 ps. The approximate focus is indicated by the red shaded holes.

A bi-directional cloak, a device that routes the path of incoming light around an object, was also studied in order to demonstrate further control over the THz waveform. The device has an inverted index profile of a lens so that it excludes light from the focal point²¹. Additional air trenches above and below the cloak (see figure 8(c) inset) allow the redirected light to be collected at the output face. Successful operation of the device can be seen by comparing the THz wave with wavelength $\lambda=260 \mu\text{m}$ interacting with a structure in the absence and presence of the cloak (see figure 8). Without the cloak, the THz wave forms a distinct far-field pattern after diffracting off the triangular air hole. In the presence of the cloak, the THz wave is routed around the object, and the resulting output retains the curvature of the input wave. As a result of diverting light around the center, the cloak operates independent of the material placed inside.

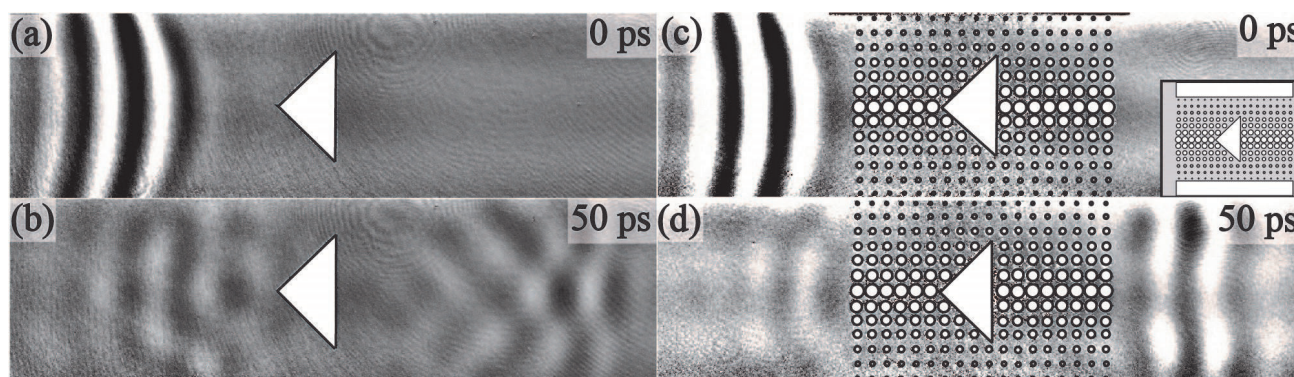


Figure 8. Cloaking of a triangular air trench for a multicycle THz wave of center wavelength $\lambda=260 \mu\text{m}$ in a $54 \mu\text{m}$ LT waveguide. The cloak excludes light from the center of the slab and uses additional air trenches on the top and bottom to recollect the light at the output. Air holes and the triangular hole have been artificially masked in white with a black border for clarity. (a) Incoming THz wave and (b) resulting diffraction pattern after interacting with a triangular air hole. (c) Incoming THz wave with inset showing the rectangular air trenches above and below cloak. (d) Well-preserved THz wave after avoiding the cloaked triangle.

6. CONCLUSION

This work represents recent advancements in the capabilities of the THz polaritonics platform. By taking advantage of these capabilities, we have been able to study the near-field interactions of THz waves with a variety of structures. The recent addition of PhCs and GRIN devices adds new levels of control to the polaritonics toolset. These devices interface seamlessly with existing polaritonics capabilities such as focusing³, field enhancement⁸, and pulse shaping of the driving femtosecond pulse¹, and could serve practical uses in possible optical processing on the polaritonics platform. In addition, the ability to utilize the electro-optic properties of the LN and LT

host materials could enable actively controllable devices that could be used for high speed optical modulation and signal processing.

ACKNOWLEDGMENTS

This work was supported by the National Science Foundation under grant no. 1128632. BKO was supported in part by an NSF GRFP fellowship and PS was supported by a Canadian Research Fellowship.

REFERENCES

- [1] Feurer, T., Stoyanov, N. S., Ward, D. W., Vaughan, J. C., Statz, E. R., and Nelson, K. A., "Terahertz Polaritonics," *Annual Review of Materials Research* **37**, 317–350 (Aug. 2007).
- [2] Dougherty, T. P., Wiederrecht, G. P., and Nelson, K. A., "Impulsive stimulated Raman scattering experiments in the polariton regime," *J. Opt. Soc. Am. B* **9**, 2179 (Dec. 1992).
- [3] Feurer, T., Vaughan, J. C., and Nelson, K. A., "Spatiotemporal coherent control of lattice vibrational waves," *Science* **299**, 374–7 (Jan. 2003).
- [4] Katayama, K., Inoue, H., Sugiya, H., Shen, Q., Toyoda, T., and Nelson, K. A., "Generation and detection of tunable phonon polaritons using a single transmission grating," *Applied Physics Letters* **92**(3), 31906 (2008).
- [5] Lin, K.-H., Werley, C. A., and Nelson, K. A., "Generation of multicycle terahertz phonon-polariton waves in a planar waveguide by tilted optical pulse fronts," *Appl. Phys. Lett.* **95**, 103304 (Sept. 2009).
- [6] Werley, C. A., Tait, R. C., and Nelson, K. A., "Direct visualization of terahertz electromagnetic waves in classic experimental geometries," *American Journal of Physics* **80**(1), 72 (2012).
- [7] Ofori-Okai, B. K., Sivarajah, P., Werley, C. A., Teo, S. M., and Nelson, K. A., "Direct experimental visualization of waves and band structure in 2D photonic crystal slabs," *New Journal of Physics* **16**, 053003 (May 2014).
- [8] Werley, C. A., Fan, K., Strikwerda, A. C., Teo, S. M., Zhang, X., Averitt, R. D., and Nelson, K. A., "Time-resolved imaging of near-fields in THz antennas and direct quantitative measurement of field enhancements," *Opt. Express* **20**(8), 8551 (2012).
- [9] Blanchard, F., Doi, A., Tanaka, T., Hirori, H., Tanaka, H., Kadoya, Y., and Tanaka, K., "Real-time terahertz near-field microscope," *Optics express* **19**, 8277–8284 (Apr. 2011).
- [10] Werley, C. A., Teo, S. M., Ofori-Okai, B. K., Sivarajah, P., and Nelson, K. A., "High-Resolution, Low-Noise Imaging in THz Polaritonics," *IEEE Trans. Terahertz Sci. Technol.* **3**, 239–247 (May 2013).
- [11] Auston, D. and Nuss, M., "Electrooptical generation and detection of femtosecond electrical transients," *IEEE J. Quantum. Electron.* **24**, 184–197 (Feb. 1988).
- [12] Amnon, Y. and Yeh, P., [*Optical Electronics in Modern Communications*], Oxford University Press, Oxford, New York, 6th ed. (2007).
- [13] Lalanne, P. and Lemerrier-Lalanne, D., "On the effective medium theory of subwavelength periodic structures," *Journal of Modern Optics* **43**, 2063–2085 (Oct. 1996).
- [14] Pendry, J. B., Aubry, A., Smith, D. R., and Maier, S. A., "Transformation optics and subwavelength control of light," *Science (New York, N.Y.)* **337**, 549–52 (Aug. 2012).
- [15] Chen, H., Chan, C. T., and Sheng, P., "Transformation optics and metamaterials," *Nature materials* **9**, 387–96 (May 2010).
- [16] Gao, H., Zhang, B., Johnson, S., and Barbastathis, G., "Design of thinfilm photonic metamaterial Lüneburg lens using analytical approach," *Optics Express* **20**(2), 3181–3186 (2012).
- [17] Brekhovskikh, L., [*Waves in Layered Media*], Academic Press (1980).
- [18] Smith, D. R., Pendry, J. B., and Wiltshire, M. C. K., "Metamaterials and negative refractive index," *Science (New York, N.Y.)* **305**, 788–92 (Aug. 2004).
- [19] Gu, C. and Yeh, P., "Form birefringence dispersion in periodic layered media," *Optics letters* **21**, 504–6 (Apr. 1996).
- [20] Hudelist, F., Buczynski, R., Waddie, a. J., and Taghizadeh, M. R., "Design and fabrication of nanostructured gradient index microlenses," *Optics express* **17**, 3255–63 (Mar. 2009).

- [21] Vasić, B., Isić, G., Gajić, R., and Hingerl, K., “Controlling electromagnetic fields with graded photonic crystals in metamaterial regime.,” *Optics express* **18**, 20321–33 (Sept. 2010).
- [22] Sivaraajah, P., Werley, C. A., Ofori-Okai, B. K., and Nelson, K. A., “Chemically assisted femtosecond laser machining for applications in LiNbO₃ and LiTaO₃,” *Applied Physics A* **112**, 615–622 (July 2013).
- [23] Garnett, J. C. M., “Colours in Metal Glasses and in Metallic Films,” *Philosophical Transactions of the Royal Society A: Mathematical, Physical and Engineering Sciences* **203**, 385–420 (Jan. 1904).
- [24] Joannopoulos, J. D., Johnson, S. G., Winn, J. N., and Meade, R. D., [*Photonic Crystals Molding the Flow of Light*], Princeton University Press, Princeton, New Jersey, 2 ed. (2008).
- [25] Yablonovitch, E., “Inhibited Spontaneous Emission in Solid-State Physics and Electronics,” *Physical Review Letters* **58**, 2059–2062 (May 1987).
- [26] John, S., “Strong localization of photons in certain disordered dielectric superlattices,” *Physical Review Letters* **58**, 2486–2489 (June 1987).
- [27] Lin, S., Chow, E., Hietala, V., Villeneuve, P. R., and Joannopoulos, J. D., “Experimental Demonstration of Guiding and Bending of Electromagnetic Waves in a Photonic Crystal,” *Science* **282**, 274–276 (Oct. 1998).
- [28] Krauss, T. F., De La Rue, R. M., and Brand, S., “Two-dimensional photonic-bandgap structures operating at near-infrared wavelengths,” *Nature* **383**, 699–702 (Oct. 1996).
- [29] Ripin, D. J., Petrich, G. S., Villeneuve, P. R., Thoen, E. R., Joannopoulos, J. D., Ippen, E. P., and Kolodziejski, L. A., “One-dimensional photonic bandgap microcavities for strong optical confinement in GaAs and GaAs/Al_xO_y semiconductor waveguides,” *Journal of Lightwave Technology* **17**(11), 2152–2160 (1999).
- [30] Peier, P., Merbold, H., Pahinin, V., Nelson, K. A., and Feurer, T., “Imaging of THz waves in 2D photonic crystal structures embedded in a slab waveguide,” *New Journal of Physics* **12**, 13014 (Jan. 2010).
- [31] Luneburg, R., [*Mathematical Theory of Optics*], University of California Press, Berkeley, 1st ed. (1964).